Influence of experimental boundary conditions on the calibration of a ductile fracture criterion

Ahmed Kacem, Hervé Laurent, Sandrine Thuillier

Influence of experimental boundary conditions on the calibration of a ductile fracture criterion

Ahmed Kacem[a,*], Hervé Laurent[a], Sandrine Thuillier[a]

[a] *Univ. Bretagne Sud, UMR CNRS 6027, IRDL, F-56100 Lorient, France*

Abstract

Hybrid experimental-numerical approach is the commonly used technique to identify the material parameters of ductile fracture criteria. In this work, attention is paid to the precise definition of the Finite Element (FE) model of fracture tests by applying real boundary conditions coming from the local displacement field. The aim is to investigate the effect of the way to reproduce experimental boundary conditions on the accuracy of the hybrid experimental-numerical approach. A stress triaxiality and Lode angle based ductile fracture criterion is used to predict the onset of ductile fracture for AA6061-T6 aluminum alloy sheets. To calibrate this criterion, a series of fracture tests is carried out up to fracture. Notched tensile specimens with different radius, tensile specimens with a central hole and shear specimens are used to cover a wide range of stress states. Strain distribution over the surface is measured with digital image correlation technique. Two numerical models are defined for each geometry type, a first one constrained with real experimental boundary conditions and a second one with ideal boundary conditions, to predict stress and strain distributions. By comparing results of both approaches with experiments, it is shown that the model constrained by

*Corresponding author

local experimental boundary conditions provides a better agreement with the experiments than the simplified model does, which underlines the sensitivity of the hybrid method to the adopted boundary conditions. Furthermore, several fracture test combinations are used to calibrate the ductile criterion and the effect of the calibration tests is discussed.

Keywords: Ductile fracture criterion, Hybrid experimental-numerical approach, Boundary conditions, AA6061-T6

Nomenclature

C_1, C_2, C_3	material parameters
D	failure indicator
D_{cri}	critical value of D
D_{pred}	predicted value of D in the critical element at the fracture stroke
E	Young's modulus
Erf	error function
f	weighting function of the stress state
L	Lode parameter
L_{avg}	average value of Lode parameter
$LE11$	longitudinal logarithmic strain

r_0, r_{45}, r_{90} plastic anisotropy coefficients

$\bar{r}$ normal anisotropy coefficient

t_f fracture time

u_{avg} average value of displacement at fracture

u_f displacement at fracture

UTS ultimate tensile strength in RD

YS yield strength at 0.2 % plastic strain in RD

δ error indicator

Δr planar anisotropy coefficient

ε_1, ε_2 logarithmic in-plane principal strain components

ε_{eq} equivalent strain

$\bar{\varepsilon}_f$ equivalent plastic strain at fracture or fracture strain

$\bar{\varepsilon}_p$ equivalent plastic strain

$\bar{\varepsilon}_{t0}$, $\bar{\varepsilon}_{s0}$, $\bar{\varepsilon}_{p0}$ fracture strains in uniaxial tension, pure shear and plane strain conditions, respectively

$\dot{\varepsilon}$ strain rate

η stress triaxiality

η_{avg} average value of stress triaxiality

ν Poisson's ratio

$\boldsymbol{\sigma}$ Cauchy stress tensor

$\bar{\sigma}$ von Mises equivalent stress

σ_1, σ_2, σ_3 principal stresses of the stress tensor

σ_m mean stress or hydrostatic stress

τ_{max} maximum shear stress

1. Introduction

Ductile fracture criteria are widely used to predict failure during manufacturing process and service. These criteria characterize the damage state in the material and when a critical value of these criteria is reached, they lead to the onset of macroscopic fracture. These criteria are expressed according to the following general form:

$$D = \int_0^{\bar{\varepsilon}_f} f(\boldsymbol{\sigma}) d\bar{\varepsilon}_p \tag{1}$$

where D is a failure indicator that indicates the onset of fracture in a given finite element when it reaches unity. $\bar{\varepsilon}_p$ is the equivalent plastic strain, $\bar{\varepsilon}_f$ is the equivalent plastic strain at fracture (or fracture strain) and f is a weighting function of the stress state represented by the Cauchy stress tensor $\boldsymbol{\sigma}$.

Several ductile fracture criteria have been developed to predict the ductile fracture of materials by using different weighting functions. Cockroft and Latham [1] proposed a fracture criterion weighted by the maximum principal

stress. Oh et al. [2] normalized the maximum principal stress in the criterion of Cockcroft-Latham by the equivalent stress. Clift et al. [3] introduced equivalent stress into the weighting function instead of maximum principal stress. Brozzo et al. [4] modified the Cockroft and Latham fracture criterion to incorporate an explicit dependence of the mean stress on the fracture strain. Rice and Tracey [5], Oyane [6], Ayada et al.[7] and Ko et al. [8] proposed fracture criteria that consider stress triaxiality. All these mentioned ductile fracture criteria have only one parameter requiring few tests to be calibrated which justifies their intensive use in industrial applications [9, 10]. However, the use of only one material parameter limits the flexibility of these criteria. Moreover, a comparative study of some ductile fracture criteria mentioned above conducted by Bao et al.[11] showed that none of them can accurately describe the fracture behavior of a given material over a large range of stress triaxialities. Barsoum and Faleskog [12] argued that the stress triaxiality is insufficient to characterize the stress state in ductile fracture. Wierzbicki et al. [13] and Gao and Kim [14] observed that predictions of ductile failure can be improved by introducing the Lode parameter. To predict fracture strain with high accuracy under a wide range of loading conditions, Bai and Wierzbicki [15, 16] have modified the Mohr–Coulomb fracture model to propose a criterion based on stress triaxiality and Lode angle. Mohr and Marcadet [17] developed the Hosford-Coulomb model accounting also for the effects of the stress triaxiality and the Lode angle. Lou et al. [18] developed a ductile fracture criterion inspired from the micro-mechanisms of ductile fracture that occurs mainly due to void nucleation, growth and finally coalescence into microcracks. It was assumed that void nucleation is proportional to the

equivalent plastic strain, void growth is controlled by the stress triaxiality and coalescence of void is dominated by the shear-linking up of voids governed by the maximum shear stress. This criterion is defined as follows:

$$D\left(\bar{\varepsilon}_p\right) = \frac{1}{C_3}\int_0^{\bar{\varepsilon}_f}\left(\frac{2\tau_{max}}{\bar{\sigma}}\right)^{C_1}\left(\frac{\langle 1+3\eta\rangle}{2}\right)^{C_2} d\bar{\varepsilon}_p \text{ with } \langle x\rangle = \begin{cases} x \text{ when } x \geq 0 \\ 0 \text{ when } x < 0 \end{cases} \tag{2}$$

where τ_{max} is the maximum shear stress, $\bar{\sigma}$ is von Mises equivalent stress. C_1, C_2 and C_3 are three material parameters that need to be calibrated by at least three different tests. η is the stress triaxiality defined as follows:

$$\eta = \frac{\sigma_m}{\bar{\sigma}} \qquad \text{with} \qquad \sigma_m = \frac{\mathrm{Tr}(\boldsymbol{\sigma})}{3} \tag{3}$$

where σ_m is the hydrostatic stress and σ_1, σ_2 and σ_3 are the principal stresses of the stress tensor, such that $\sigma_1 \geq \sigma_2 \geq \sigma_3$. Lou and Huh [19] correlated the normalized maximum shear stress to the Lode parameter, to transform the criterion into a Lode parameter dependent form:

$$D\left(\bar{\varepsilon}_p\right) = \frac{1}{C_3}\int_0^{\bar{\varepsilon}_f}\left(\frac{2}{\sqrt{L^2+3}}\right)^{C_1}\left(\frac{\langle 1+3\eta\rangle}{2}\right)^{C_2} d\bar{\varepsilon}_p \tag{4}$$

where L is the Lode parameter defined as follows:

$$L = \frac{2\sigma_2 - \sigma_1 - \sigma_3}{\sigma_1 - \sigma_3} \tag{5}$$

It should be emphasized that the three fracture parameters C_1, C_2 and C_3 should be positive as reported by Lou [20]. The fracture parameter C_1 which modulates the effect of the Lode parameter on shear coalescence of voids should have a positive value to make sure that at a constant stress triaxiality, the fracture strain in uniaxial tension (L = -1) is greater than those in plane

strain and pure shear (L = 0). The fracture parameter C_2 modulates the effect of the stress triaxiality on void growth and should also have a positive value. That is because C_2 is calculated as follows [20]:

$$C_2 = \frac{\log(\bar{\varepsilon}_{s0}) - \log(\bar{\varepsilon}_{p0})}{\log(1+\sqrt{3})} \tag{6}$$

where $\bar{\varepsilon}_{s0}$ and $\bar{\varepsilon}_{p0}$ are fracture strains respectively in pure shear and plane strain conditions. According to Eq. 6, a positive value of C_2 is guaranteed if $\bar{\varepsilon}_{s0} > \bar{\varepsilon}_{p0}$ which is true since both conditions have the same Lode parameter (L = 0) but the lower triaxiality in pure shear than that in plane strain raises the fracture strain.

The material constant C_3 modulates the magnitude of the constructed fracture locus with no influence on the shape. C_3 is positive since it corresponds to the fracture strain in uniaxial tension $\bar{\varepsilon}_{t0}$. It is worth noting that $\bar{\varepsilon}_{t0}$, $\bar{\varepsilon}_{s0}$ and $\bar{\varepsilon}_{p0}$ are fracture strains corresponding to ideal cases which cannot be achieved in practical experiments.

Lou's ductile fracture criterion have been successfully applied for predicting fracture of several metals: Dual Phase steels DP780 [18, 21] and DP980 [22], fully martensitic steel (Docol 1400M) [23], TWIP steel [24], SUS304 steel [25] and aluminum alloys AA1050 [26], AA6082-T6 [27], AA6016-T4 [28], AA2024 [18, 29] and AA7075-T6 [30, 31].

The hybrid experimental-numerical approach is widely used to calibrate the material parameters of ductile fracture criterion. In a first step, experiments are carried out using various specimen shapes to determine the instant of fracture over a wide range of stress states. Then, FE simulations of these tests are conducted to obtain the strain field and record the evolution of the

stress state during the deformation process. The fracture strain is taken as the numerical equivalent plastic strain at the displacement at rupture, coming from the experiment, and usually at the location of the maximum value, that can be within the thickness or on the surface. Due to the variation of the stress state during the test, the corresponding parameters (e.g: stress triaxiality and Lode parameter) are generally averaged. The obtained values of fracture strain and the evolution of the variables of stress state are taken thereafter to calibrate the fracture model.

A reliable FE model of experimental ductile fracture test that reproduces accurately the deformation process is strongly recommended for this approach. This can be achieved by accurately modeling the material behavior and the boundary conditions. In most of research carried out so far, efforts are focused mainly on improving the description of the material response [32, 27, 33] but no previous study has focused on the analysis of the influence of taking real boundary conditions into account in FE simulations on the calibration of fracture criterion parameters. Indeed, in most of the previous work, classical symmetrical boundary conditions was used by neglecting some effects that are likely to occur in experiments involving large deformations such as misalignment of specimen during test. Lou and Huh [22] observed that the strain distribution obtained experimentally from plane strain tensile specimens is not symmetric. Tang et al. [34] also observed that the strain distribution obtained experimentally is asymmetrical whatever the specimen shape. They claimed that it is impossible to ensure a complete alignment during the tensile test, and even a slight misalignment

will cause great rotation and asymmetry in the process of large plastic deformation. An asymmetrical strain distribution is also observed experimentally for notched specimen in the works of Lou et al. [27] and Deole et al.[23] and for plane strain tensile specimen in the work of Gruben et al. [35]. In all these cited works, authors neglected the misalignment of specimen by considering symmetric boundary conditions.

Therefore, the main objective of this work is to investigate the effect of boundary conditions on the prediction efficiency of the hybrid experimental-numerical approach. Lou's ductile fracture criterion is used to construct the fracture locus of AA6061-T6 aluminum alloy. The ductile fracture criterion is calibrated by the hybrid experimental-numerical approach. Two FE models are defined: a model constrained by reproducing the real experimental boundary conditions and a classical simplified model in which the ideal boundary conditions are applied. The effect of boundary conditions is investigated by comparing the accuracy of the parameters of the ductile fracture criterion obtained by both models. Furthermore, three sets of experiments are used to calibrate the fracture criterion. The influence of the calibration tests on the prediction accuracy is also investigated in this study.

2. Material and methods

2.1. Material

Aluminum alloy sheet AA6061-T6 with a thickness of 1 mm is considered in this work. This material is widely used in automotive applications due to

its good strength to weight ratio. AA6061-T6 fails as ductile fracture with slight necking. Therefore, ductile fracture criteria based on negligible necking such as Lou's ductile fracture criterion are more suitable to predict failure of this material [22].

2.2. Tensile test

To determine the mechanical properties, monotonic tensile tests are carried out on dog-bone specimens. Samples are designed according to ISO 6892-1 standard and manufactured using water jet cutting machine. The load is measured by a load cell of 50 kN capacity. Cauchy stress is calculated by the ratio of the load over the current section of the sample before necking. The logarithmic strain is measured by a field measuring system by 3D Digital Image Correlation (DIC) software, Aramis [36]. To prepare specimens for DIC, the sample surface is cleaned and spray-painted with a white and black stochastic pattern. Two high speed cameras equipped with 50 mm lenses are used to acquire the images for the DIC. Tensile tests are conducted under extensometer-based strain control at a constant technical strain rate of $\dot{\varepsilon} = 10^{-3}\,\mathrm{s}^{-1}$. To this end, an extensometer with a 25 mm gauge length is also used. To determine the material anisotropy, tensile tests are performed in the rolling direction (RD) as well as at 45 ° and 90 ° to RD.

2.3. Ductile fracture tests

Four types of specimens illustrated in Fig.1 are designed to obtain different stress states. Notched specimens with small (N-R5) and large (N-R15) notch radii are considered to achieve a high stress triaxiality [37]. Specimen

with a central hole (H-R4) is designed to obtain a stress state close to the uniaxial tensile test but with minor necking [38]. Finally, shear specimen (SH) is designed to achieve a low stress triaxiality [39].

All specimens are manufactured along RD using the same cutting procedure as applied for the tensile test specimens. To check the machining quality, the dimensions of specimens are measured before performing tests. Low dimensional error of about 0.02 mm is found so that the effect of the real specimen geometry can be neglected. To assess the repeatability of the experiments, three samples are prepared for each geometry. All experiments are carried out using a universal testing machine INSTRON 5969 under displacement control at a constant crosshead velocity. For each type of specimen, the crosshead speed is set to obtain an average strain rate of about $\dot{\varepsilon} = 10^{-3}\,\mathrm{s}^{-1}$, which is the same value as in uniaxial tensile test. It should be emphasized that strain rate control can not be used in ductile fracture test since the deformation is not homogeneous in the gauge length area of the extensometer. The deformation evolution during experiments is recorded using the DIC Aramis, with the same parameters as in the tensile test. The three tests for each type of specimen lead to at least two ones with quite similar results. One test is selected for each specimen geometry to determine the corresponding fracture strain and stress state. It should be noted that in real experimental situations, the common practice is to choose the test showing the least source of error. In this work, the same practice is adopted to show that even when working in real experimental conditions the misalignment may affect the obtained results.

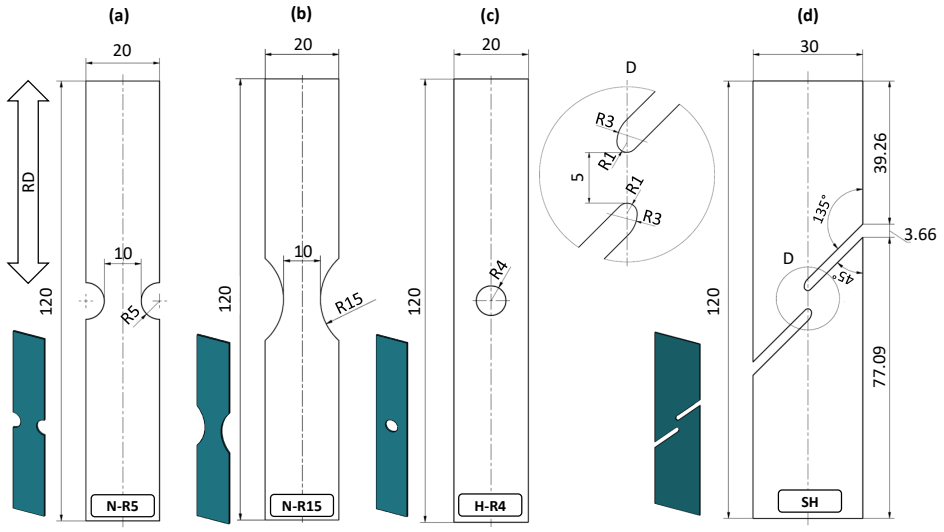

Figure 1: Geometry and dimensions (in mm) of the four specimens designed to obtain different stress states: (a) notched specimen with R = 5 mm (N-R5) (b) notched specimen with R = 15 mm (N-R15) (c) specimen with a central hole with R = 4 mm (H-R4) (d) shear specimen (SH).

In order to quantify the misalignment of the sample during the test likely to occur in this kind of experiments, by Aramis, five virtual extensometers with a gauge length of 15 mm are defined at different positions and the evolution of the displacements of these extensometers in function of the normalized time is recorded. A representative result is shown in Fig.2 for the testing of a specimen with a central hole. It can be seen that the displacement at fracture u_f strongly depends on the position of the extensometer. Therefore, the values are averaged and the displacement at fracture u_f corresponds to the averaged displacement u_{avg} at the fracture time t_f. It is worth noting that the fracture time is identified as the time when a sudden drop in the

measured load-displacement curve is recorded.

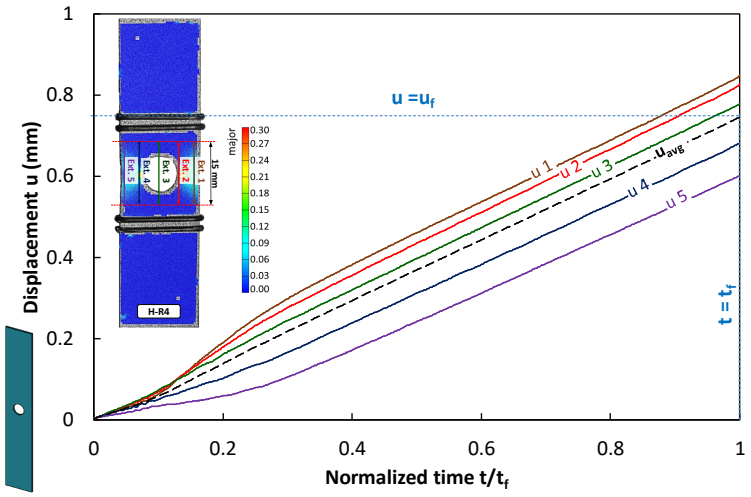

Figure 2: Evolution of displacement of the five virtual extensometers (gauge length of 15 mm) defined at different positions with Aramis as a function of time t normalized by the fracture time t_f, for a specimen with central hole H-R4.

2.4. FE modeling

Numerical simulations of the different fracture ductile tests and the tensile test are performed in 3D with the FE code Abaqus/Standard. Attention is paid to develop a FE model as close as possible to the experimental conditions. For that reason, a full model of the specimen is defined to account for all possible displacements of specimen during the test. In addition, only the part of the specimen between the grips of the tensile machine is modeled in such a way that the length of the specimen in the FE model is almost equal to the distance between the grips of the tensile machine as shown in Fig.3. The specimens are discretized by 3D solid hexahedral elements with

reduced integration (C3D8R). Since reduced integration is used, the hourglass control based on the total stiffness approach used by default in Abaqus is employed. Mesh with a size of approximately 0.2 mm in the local zone where strain localization is likely to occur (see the zooms in Fig.3), and with larger size at sections away from this zone is used. Since the local zone of the shear specimen is smaller than that of the other geometries, a smaller mesh size of about 0.1 mm is used for this specimen. All the models have 6 elements through the thickness. Dunand and Mohr [38] have shown that the prediction of force–displacement relationship is approximately mesh size independent, but the mesh density has a noticeable effect on the predicted fracture strain. Therefore, the size of elements is determined based on convergence of the fracture strain. Indeed, simulation are carried out with 2, 4, 6 and 8 elements through the thickness. It is found that results converge when the element number is larger than 6. For the tensile test, since experimentally the fracture was initiated from the edge, a tiny imperfection (0.03 mm) has been done in the FE model geometry to trigger numerically the deformation localization also on the edge.

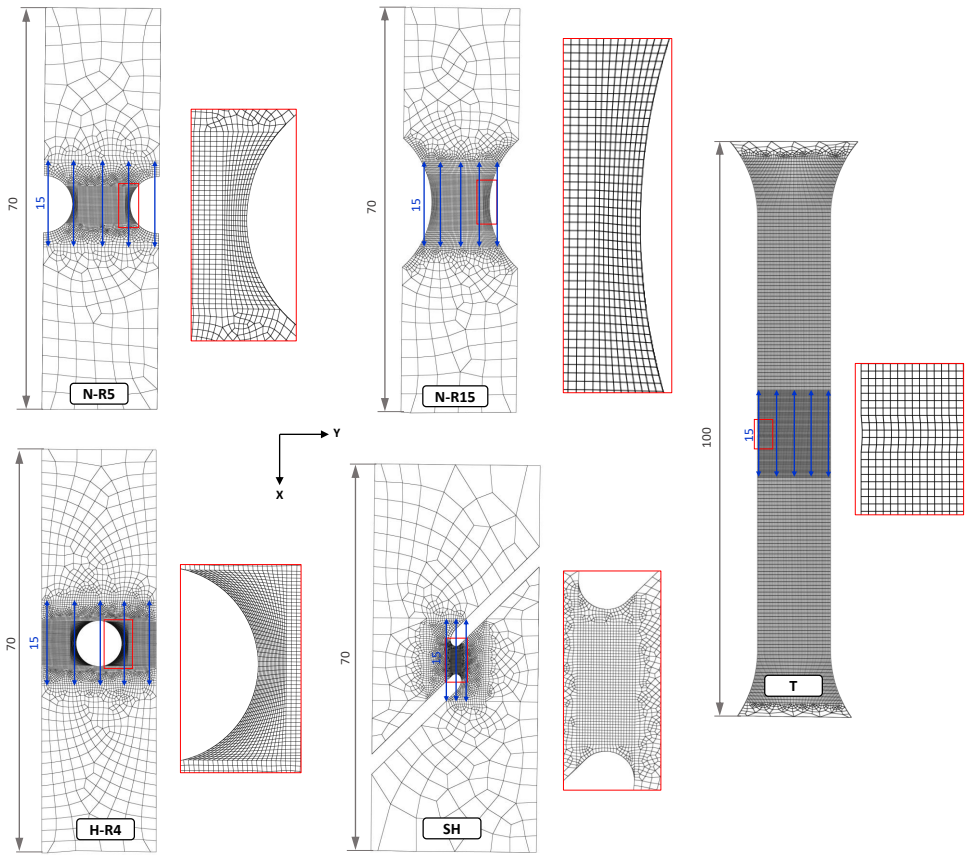

Figure 3: Meshes used for the four ductile fracture tests and the tensile test. In red, zooms on the meshes in zones where strain localization is likely to occur. The blue dimension lines highlight the position of the virtual extensometers with gauge length of 15 mm used for local displacement measurement.

The boundary conditions are applied in two different ways. For the first case (model M1), non-zero displacements (U_x, U_y and U_z) are imposed on the lower and upper sides of specimen as shown in Fig.4-a. These values are obtained from the displacement field recorded by Aramis on the specimen surface. An automatic procedure is developed to apply the experimental lo-

cal displacements to the FE model with a Python script. Such a procedure leads to a more realistic model, in which the misalignment of the specimen during the test is reproduced. For the second case (model M2), the nodes located on the lower side are clamped while those located on the upper side are moved along X axis with a smooth increasing displacement as shown in Fig.4-b. In this case, the model is simplified by assuming a perfect alignment of the specimen during the test and considering the conditions of a homogeneous tensile test. For both models, five virtual extensometers with a gauge length of 15 mm are defined at the same positions of those used with Aramis as explained before, to output a local displacement used to plot the load evolution. Note that only three virtual extensometers are defined for shear specimen as shown in Fig.3.

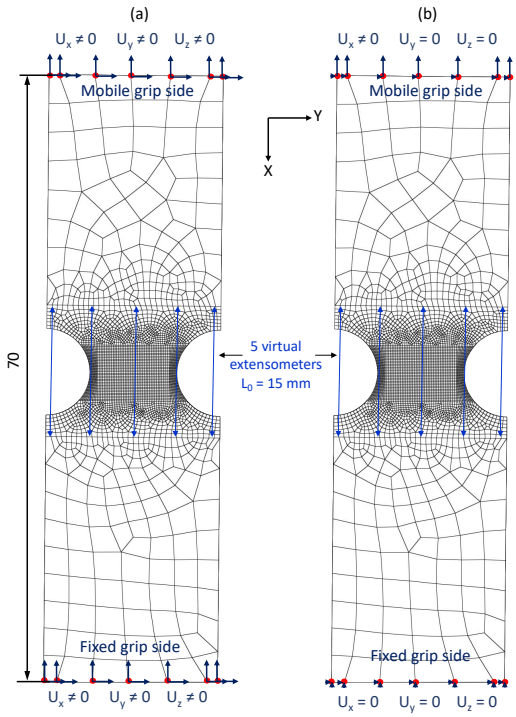

Figure 4: Boundary conditions used for (a) the representative experimental conditions test (Model M1) and (b) assuming a perfect alignment of specimen (Model M2). Red dots represent nodes where boundary conditions are applied.

To model the mechanical behavior, the aluminium alloy is assumed to have an elastic-plastic behavior with an isotropic hardening rule. The anisotropy is neglected in a first step. The material is assumed to be isotropic and to obey the von Mises yield criterion. Before necking, the hardening curve is obtained from the uniaxial tension test detailed in section 2.2. After necking, the hardening curve is described by a linear piecewise relation identified by a manual inverse method that consists of manually adjusting the hardening curve while visually inspecting the agreement between the experimental and

predicted results as detailed in section 3.1. Indeed, the hardening curve is adjusted so that the simulation provides an accurate prediction of the experimentally measured force-displacement curve, as described by Dunand and Mohr [38] and Kacem et al. [40]. The material model is already implemented in Abaqus, with the hardening law defined in a tabular form, and the failure criterion is not incorporated in a first step.

2.5. Calibration methodology

The hybrid experimental-numerical method is applied to calibrate the fracture model. Normally the fracture strain is defined as the equivalent plastic strain in the first element (integration point) with a failure indicator D reaching the unity. However, the failure indicator is affected by fracture parameters C_1, C_2 and C_3 which are to be identified from experimental results first. This element cannot be located since the fracture parameters have not been identified yet. Therefore, it is assumed that the fracture initiates in the element with the highest equivalent plastic strain at the instant of fracture t_f (critical element). The fracture strain $\bar{\varepsilon}_f$ corresponds thus to the maximum equivalent plastic strain at the fracture stroke u_f. This assumption has been proved in previous works. Talebi-Ghadikolaee et al. [41] have shown that for sheet notched specimens the position of the element with the highest equivalent plastic strain is the same as that of the element with highest failure indicator value. Lou and Huh [22] found that for specimen with central hole and shear specimen the element with the maximum fracture indicator is close to that with the largest equivalent plastic strain. They also claimed that identification method based on this assumption provides sufficient approximation of fracture parameters. Therefore, to determine the fracture strain,

the displacement at fracture u_f is first determined experimentally. Then, the maximum equivalent plastic strain is extracted from the numerical simulation of ductile fracture test at the corresponding experimental fracture stroke u_f. Simultaneously, evolution of stress triaxiality η and Lode parameter L is obtained from the numerical analysis. Although, specimens are designed to achieve a constant stress state, η and L may vary during test. Therefore, to assign a specific stress to each fracture test it is convenient to calculate the average of stress triaxiality η_{avg} and Lode parameter L_{avg} by the following relations:

$$\eta_{avg} = \frac{1}{\bar{\varepsilon}_f} \int_0^{\bar{\varepsilon}_f} \eta \, d\bar{\varepsilon}_p \quad \text{and} \quad L_{avg} = \frac{1}{\bar{\varepsilon}_f} \int_0^{\bar{\varepsilon}_f} L \, d\bar{\varepsilon}_p \tag{7}$$

A Python script is developed for the presented methodology. It makes it possible to determine ($\bar{\varepsilon}_f$, η_{avg}, L_{avg}) for each specimen in the post-processing phase.

The failure indicator D at the critical element can be calculated for each test through Eq.4 by using the loading history extracted from the numerical simulation of the tests and the fracture strain $\bar{\varepsilon}_f$ determined by the hybrid approach. Therefore, to calibrate the fracture criterion, the fracture parameters are optimized using a generalized reduced gradient (GRG) algorithm tool by minimizing the following error function defined in the least square sense.

$$Erf = \sum_{i=1}^{N_s} (1 - D_i)^2 \tag{8}$$

where N_s denotes the number of samples used for the calibration and D_i corresponds to the failure indicator of the i^{th} test which is calculated numer-

ically through Eq.4.

Three sets of experimental data are used to calibrate the fracture criterion: set 1 (SH, H-R4 and N-R5), set 2 (SH, H-R4 and N-R15) and set 3 (SH, H-R4, N-R15 and N-R5). For sets 1 and 2 the minimum number of tests ($N_s = 3$) required to identify the fracture parameters is used whereas for set 3 all fracture specimens ($N_s = 4$) are employed for calibration. It should be noted that dog-bone specimen is not utilized for calibration and serves mainly the purpose of validation.

3. Results and discussion

3.1. Mechanical behavior in uniaxial tension and hardening

Fig.5 shows the Cauchy stress-logarithmic strain curves obtained in uniaxial tension, with dog-bone specimen. It can be seen that there is no significant difference on the stress level according to the different orientations of the tensile test compared to RD. The mechanical properties are given in Tab.1. The measurement of both transverse and longitudinal strains leads to the plastic anisotropy coefficients r_α, for $\alpha = 0, 45, 90°$, also given in Tab.1. It can be seen that the normal anisotropy coefficient $\bar{r}$ is significantly different from 1 but the planar anisotropy coefficient Δr is rather weak.

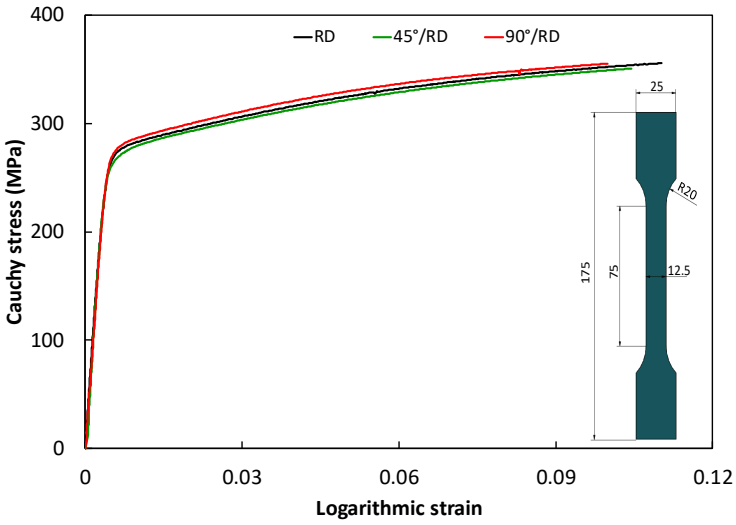

Figure 5: Cauchy stress-logarithmic strain curves in uniaxial tension obtained with dog-bone specimen up to the point of necking at 0°, 45° and 90° to the RD. Sample dimensions are given in mm.

E (GPa)	ν	YS (MPa)	UTS (MPa)	r_0	r_{45}	r_{90}	$\bar{r}$	Δr
70	0.33	270	318	0.59	0.78	0.81	0.74	-0.08

YS Yield Strength at 0.2 % plastic strain in RD **UTS** Ultimate Tensile Strength in RD

Table 1: Mechanical properties and anisotropy coefficients of AA6061-T6.

Fracture usually occurs at high strain levels, well beyond necking. Therefore, an accurate description of hardening after necking and up to fracture is fundamental in the hybrid experimental-numerical approach. Tarigopula et al. [42] claimed that the shear specimen is more suitable to determine strain hardening for large stains since it could undergo large deformation without necking. For this, the hardening curve is extrapolated manually using the

shear specimen which was also used by Lou and Huh [22], Tang et al. [34] and Quach et al. [43]. Indeed, the stress-strain curve used as material input is continually adjusted until the numerical and experimental load-displacement curves obtained with the shear specimen (SH) show good agreement. The finally determined stress-strain curve is utilized to describe the strain hardening behavior beyond necking in the FE models of all specimens. Though the comparison between tension and shear stress levels may depend on an anisotropic yield criterion, it is observed that this choice, associated to von Mises yield criterion, gives a good description of the fracture test load level. Fig.6 shows the hardening curve beyond necking modulated by the manual inverse engineering method.

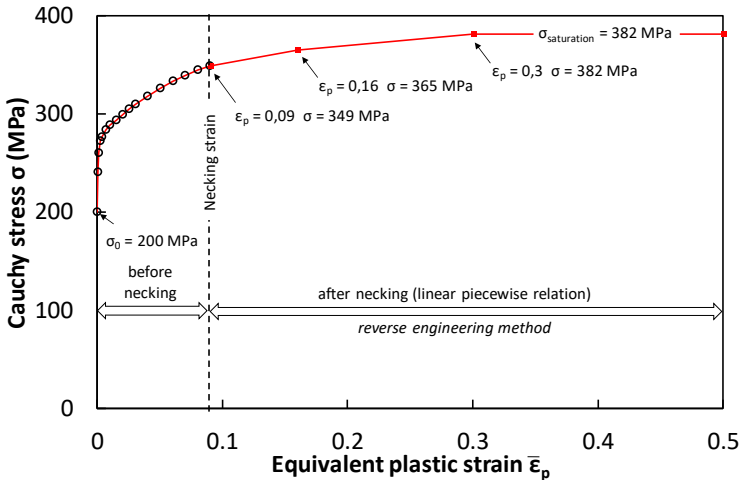

Figure 6: Hardening curve (in red) obtained from stress-strain curve using uniaxial tension of dog-bone specimen before necking and by a reverse engineering method using shear specimen after necking. Black circles represent experimental points obtained from uniaxial tension of dog-bone specimen.

3.2. Accuracy of FE model

To verify the FE models, Fig. 7 shows the load-local displacement curves obtained both numerically with M1 and M2 models and experimentally. The local displacement is measured based on the five extensometers with 15 mm gauge length as depicted in Fig.4.

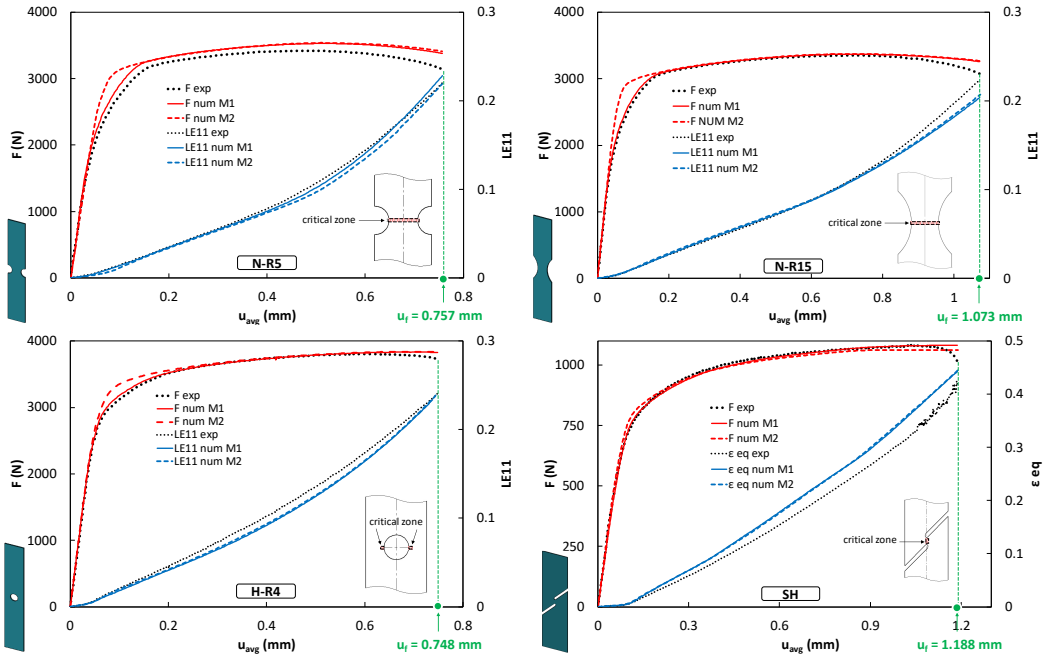

Figure 7: Comparison of the load-local displacement curves and the evolutions of average strain at the critical zone where fracture initiates (longitudinal logarithmic strain LE11 for N-R5, N-R15 and H-R4 specimens and the equivalent strain ε_{eq} for SH specimen) between numerical and experimental results. Vertical dashed green lines depict the displacement at fracture u_f.

It can be seen that the numerical results obtained with M1 and M2 models fit well the experimental data, not only with the shear test used for hardening

extrapolation but also for all other tests. In the case of notched specimen N-R5, the numerical simulation overestimates slightly the load. This may be due to the dependency of the hardening behavior to the stress state that was ignored in the numerical simulation. Fig.7 shows also the numerical and experimental evolution of the average longitudinal logarithmic strain LE11 at the surface of the critical zone for each specimen. For the shear specimen, the equivalent strain ε_{eq} (Eq.9) is used out of comparison's sake [36].

$$\varepsilon_{eq} = \frac{2}{\sqrt{3}}\sqrt{\varepsilon_1^2 + \varepsilon_2^2 + \varepsilon_1\varepsilon_2} \tag{9}$$

where ε_1 and ε_2 are the logarithmic in-plane principal strain components.

As expected, the load-local displacement responses between M1 and M2 models show that numerical results with model M1 are closer to the experimental results than those predicted by model M2. The difference between both models is mainly observed for N-R5, N-R15 and H-R4 specimen, at the beginning of the test. Indeed, the effect of misalignment on the test kinematic is more significant at the early stage of the test, characterized by a different velocity between the five extensometers as can be seen in Fig.2. Moreover, the misalignment causes higher stress concentration at the beginning of the test leading to an early onset of plasticity which can be predicted by model M1. Therefore the linear evolution in the load-displacement curve linked to the elastic deformation at the beginning of test is more rapidly lost by model M1. Comparison also shows that strain evolution predicted by model M1 is similar to that predicted by model M2 in the case of specimens N-R15, H-R4 and SH. For specimens N-R5 a minor difference is observed.

The numerical simulations are further verified by comparing the experimental and numerical major strain distribution on the specimen surface just before fracture, as reported in Fig. 8. The misalignment of specimen during test leads experimentally to an asymmetrical strain distribution that is also well predicted by the numerical model M1. Even though numerical model M2 does not consider the misalignment of specimen, it shows a comparable strain magnitude but the distribution is less well reproduced. For notched specimens N-R5 and N-R15, the maximum major strain recorded by Aramis is found between the center of specimen and the edge of the notch. The maximum value is located closer to the edge for N-R5 specimen and closer to the center for N-R15 specimen. This observation is also predicted by model M1 with a slight shift of maximum value towards the center. However, for model M2 the maximum major strain is usually found at the center for both specimens. For H-R4 specimen, it is observed that the major strain is more concentrated on the right side of the hole edge that is also well predicted by model M1. Note that the large deformation at the edge cannot be calculated by DIC method so that the maximum value of major strain measured by Aramis is smaller than that predicted by FE model. For shear specimen, much higher strain level is obtained. It can be clearly seen that both models exhibit similar results and are in excellent agreement with experimental observations. In this case, the maximum major strain is located close to the edge where fracture experimentally initiates.

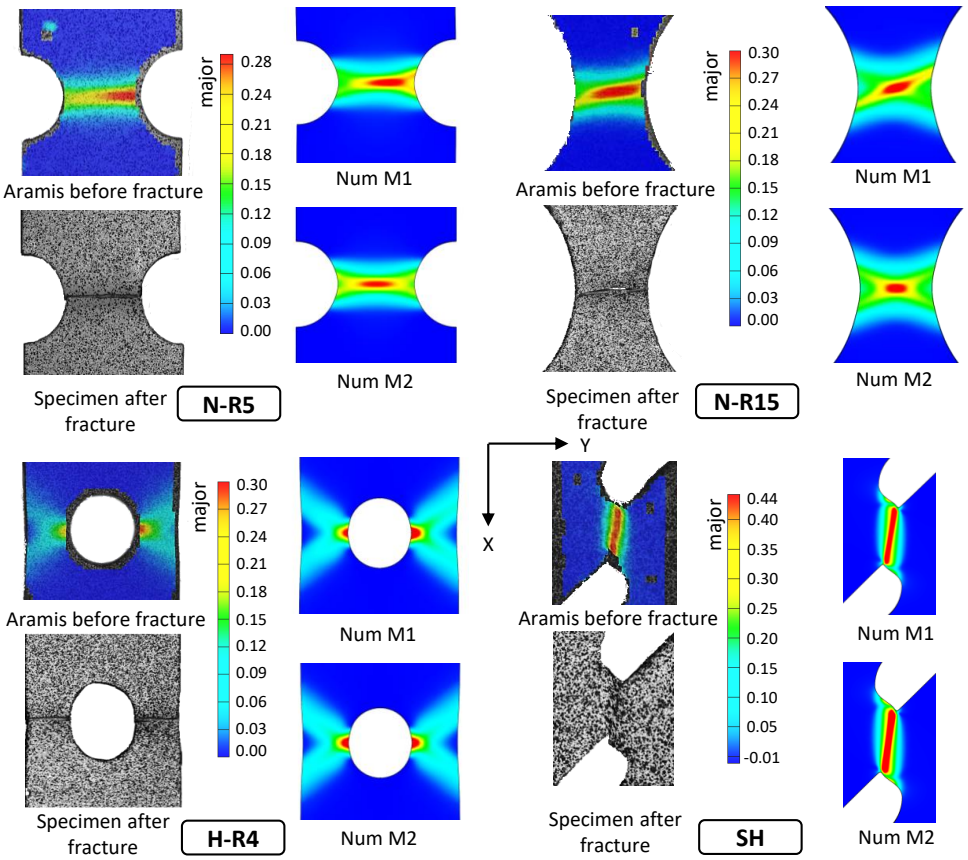

Figure 8: Comparison of major strain distributions on the specimen surface between Aramis and simulation just before fracture and specimens after fracture tests. The fracture strain is located within the thickness for N-R5, N-R15 and H-R4 specimens and at the centre of shear gauge for SH specimen.

The reliability of simulation is then quantitatively verified by comparing the evolution of major strain along longitudinal and transverse directions passing through the element with maximum major strain recorded by Aramis at fracture, as depicted in Fig. 9. It can be seen that the shape of the numerical and experimental curves are broadly similar. The simulations with

model M1 better correlated with the experiments than those with model M2 for all types of specimen considered. In the case of notched specimens, a divergence is seen between numerical and experimental results for high values of displacement u. At final stage ($u = u_f$), the maximum major strain in transverse position is located experimentally at 3.24 mm and 0.73 mm away from the center of N-R5 and N-R15 specimens, respectively. The relative error in the location of maximum major strain in transverse position predicted by models M1 and M2 for notched specimen N-R5 is 25 % and 43.5 %, respectively and 12.4 % and 18.8 % for notched specimen N-R15, respectively. However, in terms of maximum major strain value a good agreement between experimental and numerical results is observed. The relative error on this strain value does not exceed 6.5 % and 3.2 % for notched specimens N-R5 and N-R15, respectively. In the case of specimen with central hole, the major strain is more rapidly concentrated at the localized zone than the other specimens. At the early stage ($u = 1/4\, u_f$) the difference between the maximum and minimum experimental major strain values along the transverse direction is found about 0.043 which is much higher than those observed for notched specimens N-R5 and N-R15 of about 0.04 and 0.027, respectively. Numerically, the relative error on this value predicted at this stage for H-R4 specimen by models M1 of about 2.5 % is lower than that predicted by model M2 of about 41.9 %. Furthermore, the relative errors on this value predicted at this stage for N-R5 and N-R15 specimens by model M1 of about 6.5 % and 22.5 %, respectively are also lower than those predicted by model M2 of about 79.4 % and 67 %, respectively. The large difference between experimental and numerical results with model M2 observed in this case is due

to the misalignment of specimen leading to an early strain concentration at the edge of the notch that cannot be predicted by model M2. In the case of shear specimen, the major strain values exhibit low variation along the longitudinal direction. At the half of loading process ($u = 1/2\, u_f$), the relative difference between the maximum and minimum values is found numerically with models M1 and M2 of about 12 % and 13 %, respectively. At the final stage ($u = u_f$), the relative difference increases numerically to 30 % and 29 % for models M1 and M2, respectively but it remains experimentally constant. The difference between numerical and experimental results observed in this case may be due to the lack of experimental major strain values at the edge of the specimen where fracture initiates since Aramis cannot calculate precisely the strain at this location.

In conclusion, the comparison between numerical and experimental results indicate that the numerical simulation is reliable to describe the plastic deformation of all types of specimens. Besides, as expected, numerical simulations with M1 describe more precisely the deformation distribution of fracture tests and seem therefore more suitable to calibrate the fracture criterion.

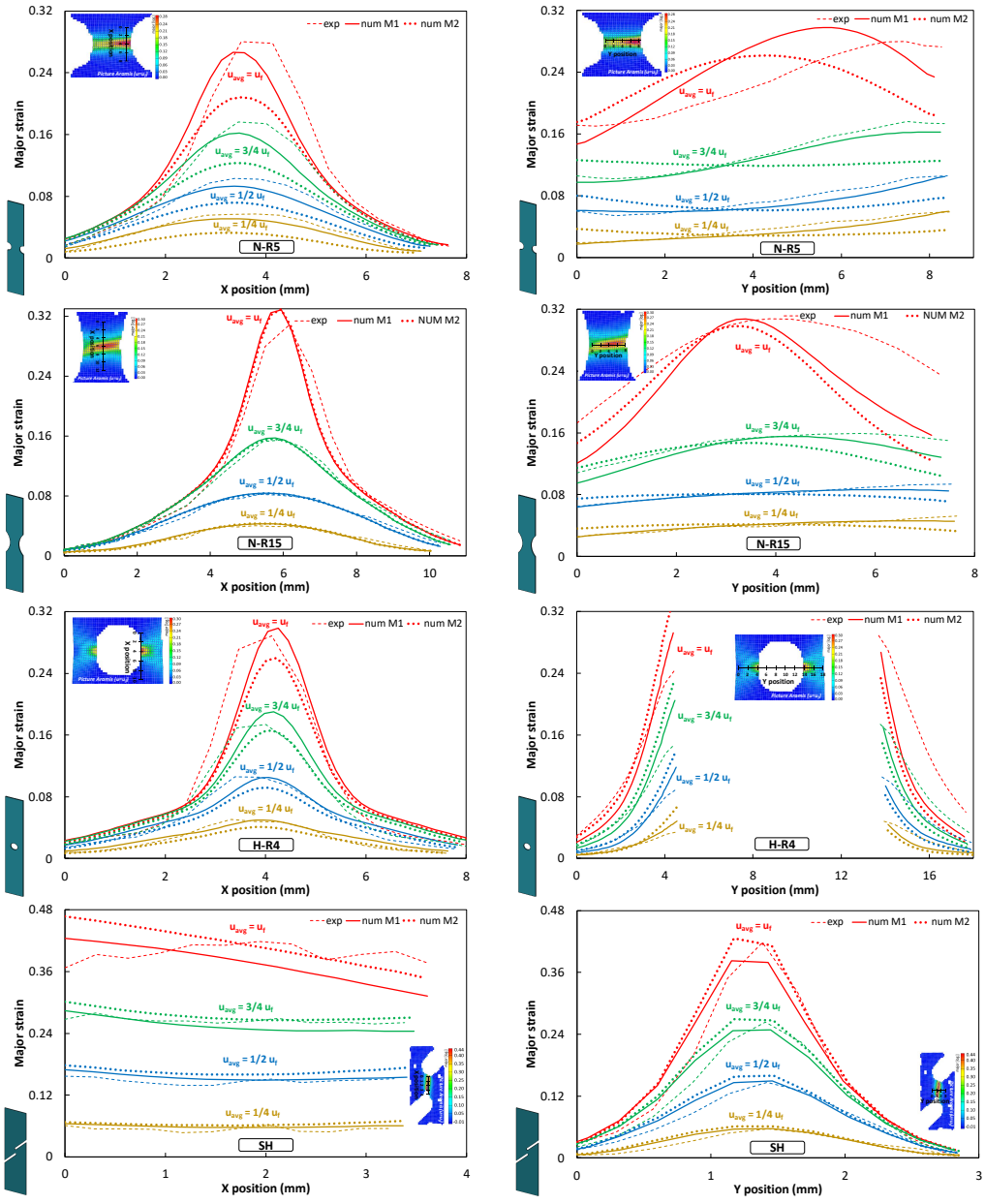

Figure 9: Evolution of major strain with X position along longitudinal direction (left) and Y position along transverse direction (right) for different local displacements, for all fracture tests. Results are taken from the nodes located along longitudinal and transverse directions passing through the element with maximum major strain recorded by Aramis.

3.3. Prediction of ductile fracture

The hybrid experimental-numerical approach is used to predict the fracture strain and the average triaxiality and Lode parameter for each type of test. The local displacement at fracture u_f is first determined experimentally, as shown in Fig.7. Numerically, the element presenting the maximum equivalent plastic strain at u_f (critical element) is located in the center of specimen, within the thickness for N-R5, N-R15 and H-R4 specimens. In the case of shear specimen, due to edge effect the maximum equivalent plastic strain at u_f is found at a point close to the edge rather than at the center. The critical element cannot be taken at the edge since the stress state is not a one of shear in this region. Therefore, the equivalent plastic strain at the center of the shear gauge is chosen as the fracture strain. This assumption was broadly applied in previous works [22]. To avoid edge effect in pure shear butterfly specimen proposed by Mohr and Henn [44] is recommended. However, this type of specimen cannot be used for thin sheets since it needs through-thickness machining. Evolution of stress triaxiality and Lode parameter at the critical element is obtained from the numerical analysis as shown in Fig.10.

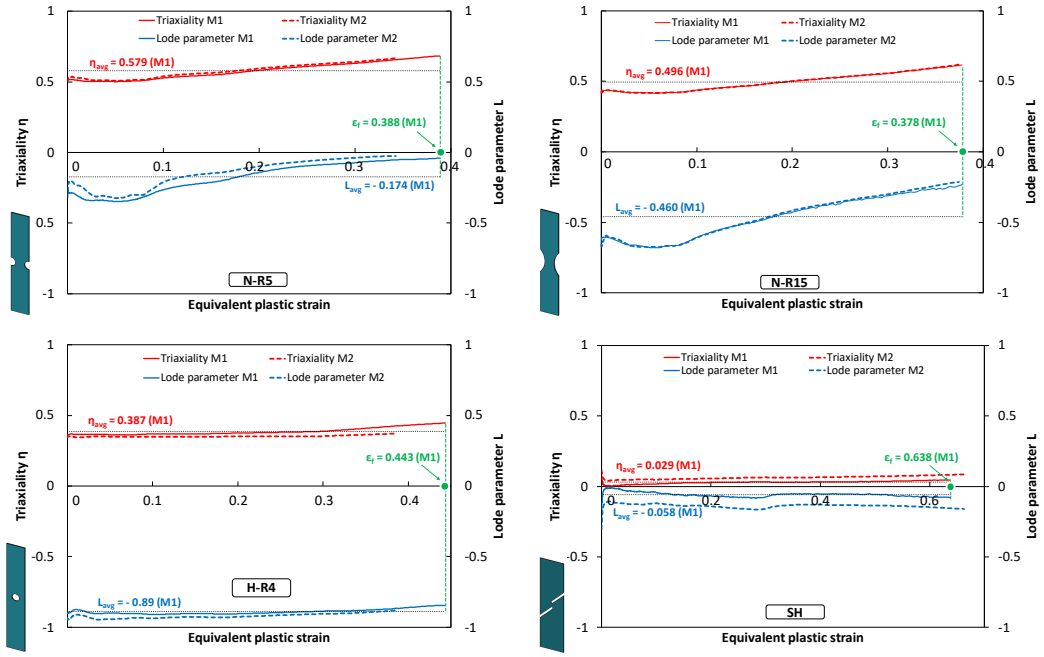

Figure 10: Evolution of stress triaxiality and Lode parameter at the critical element corresponding to the element presenting the maximum equivalent plastic strain at u_f for N-R5, N-R15 and H-R4 specimens and selected at the center of the shear gauge for SH specimen for models M1 and M2. Horizontal dashed black lines show average triaxiality η_{avg} and Lode parameter L_{avg} while vertical dashed green line depicts the fracture strain only for model M1 for clarity purpose.

It is found that the values of triaxiality and Lode parameter calculated for N-R5 and N-R15 specimens are not stable and exhibit significant variation during plastic deformation. This is due to the localized necking leading to the development of out of plane stress components in the critical zone that increases the stress triaxiality and modifies the evolution of Lode parameter. In the case of SH and H-R4 specimens small variations of triaxiality and

Lode parameter are obtained since these specimens are characterized by minor necking. For instance, for notched specimen N-R15 the Lode parameters values predicted by model M1 varies between -0.714 and -0.232 corresponding to an absolute difference of 0.482 while those predicted by the same model for H-R4 specimen varies between -0.911 and -0.845 corresponding to an absolute difference of 0.066. The absolute difference in stress triaxiality predicted by model M1 for N-R15 and H-R4 specimens are respectively 0.21 and 0.087.

Triaxiality and Lode parameter variation obtained by models M1 and M2 are also compared in Fig.10. It can be seen that both variations are similar in the case of N-R15 specimen but slightly different for other fracture test specimens. The largest difference is observed in the Lode parameter of SH specimen.

The average stress triaxiality η_{avg} and Lode parameter L_{avg} are then calculated according to Eq. 7. The values of fracture strain $\bar{\varepsilon}_f$ and the corresponding average triaxiality η_{avg} and Lode parameter L_{avg} are listed in Tab.2. The average triaxiality η_{avg} and Lode parameter L_{avg} are also included with dashed lines in Fig.10 only for model M1 for clarity purpose.

		$\bar{\varepsilon}_f$	η_{avg}	L_{avg}
N-R5	Model M1	0.388	0.579	-0.174
	Model M2	0.342	0.578	-0.148
N-R15	Model M1	0.378	0.496	-0.460
	Model M2	0.372	0.497	-0.455
H-R4	Model M1	0.443	0.387	-0.890
	Model M2	0.387	0.353	-0.920
SH	Model M1	0.638	0.029	-0.058
	Model M2	0.663	0.063	-0.138

Table 2: Fracture strain and the corresponding average stress triaxiality and Lode parameter.

It can be seen that fracture strain predicted by model M2 is lower than that predicted by model M1 for specimens N-R5, N-R15 and H-R4. The difference is about 13 % for specimens N-R5 and H-R4 and 2 % for specimen N-R15. For SH specimen, a minor difference of fracture strain between both models of about 4 % is observed. Regarding the stress state, it is found that η_{avg} and L_{avg} values are almost similar for both models of specimens N-R5, N-R15 and H-R4. However, a significant difference is observed in case of SH specimen. Indeed, the average values obtained from model M1 are closer to the pure shear state ($\eta = 0$ and $L = 0$) than those obtained from model M2.

3.4. Determination of fracture locus

Since the loading paths are non-linear, the values of $\bar{\varepsilon}_f$, η_{avg} and L_{avg} determined by the hybrid experimental-numerical approach are firstly used to estimate an initial guess of the material parameters C_1, C_2 and C_3 of Lou's fracture criterion. Then the final values of fracture criterion parameters are obtained by using the integral expression for the non-linear loading path according to Eq.4 to construct the fracture locus of AA6061-T6 aluminum alloy.

Three sets of calibration tests are used to calibrate the fracture criterion as explained in section 2.5. Tab.3 shows the calibration results for models M1 and M2. It should be noted that results obtained by model M2 with all sets are not realistic since they lead to negative values of fracture parameters. For that reason, the calibration for model M2 is performed otherwise by constraining C_1, C_2 and C_3 to be positive and only set 3 is considered in this case.

It is found that the calibration result depends strongly on the set of experiments used for calibration that was also concluded in previous works by Deole et al.[23] and Yang et al.[30]. The low value of C_1 obtained in most of the cases means that the Lode parameter has a weak effect on the fracture strain. This was also observed for DH36 steel [45], 5083-H116 aluminum alloy [46] and 5083-O aluminum alloy [47]. Moreover, since the material used in this work exhibits a weak Lode parameter dependency, the calibration of a Lode parameter dependent ductile fracture criterion may fail for this material mainly when it is used with the ideal model M2. This highlights again the importance of considering the real boundary conditions in the simulation of fracture test.

		C_1	C_2	C_3
M1	set 1	0.0538	0.5383	0.4627
	set 2	0.8076	0.6661	0.4768
	set 3	0.1588	0.5725	0.4593
M2	set 3	0	0.7887	0.4306

Table 3: Calibrated fracture parameters with the three sets of experiments for model M1 (set 1 (SH, H-R4 and N-R5), set 2 (SH, H-R4 and N-R15) and set 3 (SH, H-R4, N-R15 and N-R5)) and with set 3 for model M2.

An error indicator δ is used to evaluate the prediction accuracy of material parameters obtained by each set:

$$\delta = \frac{|D_{cri} - D_{pred}|}{D_{cri}}.100\% \tag{10}$$

where D_{cri} is the critical value of D which is supposed to be unity in this work and D_{pred} is the value of D in the critical element at the fracture stroke.

Tab.4 shows the prediction error for models M1 and M2. For model M1, low values of mean error are obtained for all sets of experiments. The minimum mean error of 1.91 % is obtained by using the first set of calibration tests. It is also found that calibration with model M2 leads to an acceptable mean error of 3.82 % but it remains higher than that predicted by model M1 using the same set of experiments (2.49 %). It should be noted that the prediction error for model M2 can be calculated otherwise by setting the real model M1 as a reference. In this case the failure indicator D is calculated by using the FE model of M1 in which the fracture parameters calibrated by

model M2 are incorporated. The mean error obtained in this case is 9.39 % which is very higher than those predicted by model M1. This indicates that real model M1 should be considered to calibrate ductile fracture criterion with high accuracy.

			N-R5	N-R15	H-R4	SH	T (validation)
M1	set1	D_{pred}	1	0.924	1	1	0.984
		error (%)	-	7.64	-	-	1.57
		mean error (%)	1.91				-
	set2	D_{pred}	1.12	1	1	1	1.004
		error (%)	12.04	-	-	-	0.43
		mean error (%)	3.01				-
	set3	D_{pred}	1.033	0.948	1.013	1.002	1.0002
		error (%)	3.32	5.18	1.3	0.17	**0.02**
		mean error (%)	**2.49**				-
M2	set3	D_{pred}	1.018	1.033	0.919	1.021	1.072
		error (%)	1.79	3.32	8.07	2.11	7.23
		mean error (%)	3.82				-

Table 4: Failure indicator D predicted in the critical element at the fracture stroke and prediction errors (Eq.10) of the three sets of experiments for model M1 and of set 3 for model M2.

Fig.11 shows the locus of fracture strains in the 2D space (η, $\bar{\varepsilon}^p$) under the plane stress condition. The (η_{avg},$\bar{\varepsilon}_f$) points obtained by the hybrid experimental approach using models M1 and M2 are superimposed in Fig.11. It can be seen that the fracture locus is strongly dependent on the used model and calibration tests which witness the high sensitivity of the hybrid

experimental-numerical approach to the boundary conditions adopted and to the set of tests used for calibration. Comparison between both models reveals that model M1 fits more accurately the results obtained by the hybrid approach. Therefore, it can be concluded that model M1 is more suited than model M2 for the calibration of ductile fracture criterion.

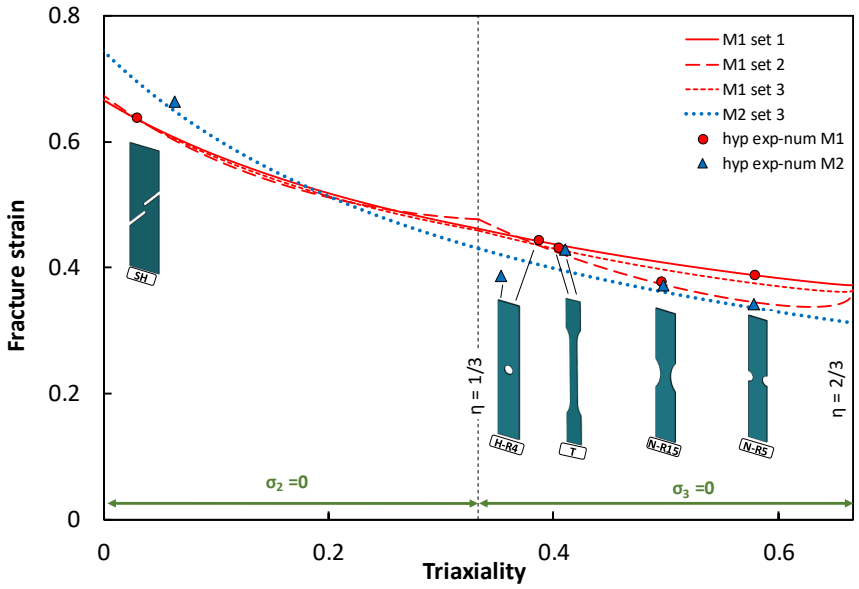

Figure 11: Fracture locus constructed in the space (η, $\bar{\varepsilon}^p$) under the plane stress condition using model M1 (set 1, set 2 and opt) shown with red lines and model M2 (opt) shown with blue line. The (η_{avg},$\bar{\varepsilon}_f$) points obtained by the hybrid experimental-numerical approach using models M1 and M2 are shown with red and blue dots, respectively.

It can also seen that for N-R15 specimen data points obtained by the hybrid approach by both models are very close to each other. The effect of considering the real boundary conditions in N-R15 specimen seems to be

lower than other specimens as can also seen in Fig. 7,9 and 10. Therefore N-R15 specimen is not really interesting to accurately model the real boundary conditions and could be replaced by other specimen (e.g N-R10).

3.5. Validation of fracture locus

Tensile tests on dog-bone shaped specimens are used for validation. Fig.12 shows the numerical and experimental force-displacement curves. It should be noted that both models M1 and M2 predict similar result of the force-displacement curve. For that reason, only the numerical curve predicted by model M1 is presented in Fig.12 for clarity purpose. Good agreements between experimental and numerical results is observed which verified the FE models. Fig.12 shows also the longitudinal logarithmic strain LE11 distributions on the specimen surface just before fracture obtained experimentally by Aramis and numerically by Models M1 and M2. It is obvious that both models predict accurately the location of necking zone observed in this case at the edge which demonstrates the reliability of the FE models. It is also found that the strain distribution predicted by model M1 is closer to the experimental strain distribution than that predicted by model M2 which confirms once again that model M1 is more suitable to calibrate the fracture criterion.

The $(\eta_{avg},\bar{\varepsilon}_f)$ points obtained by the hybrid experimental approach using models M1 and M2 are superimposed in Fig.11. The data point obtained by the hybrid approach using model M1 is closer to the fracture locus than that obtained using model M2. The prediction errors are reported in Tab.4. For all sets of experiments the prediction error is smaller than 1.57 % for model M1. The error is close to zero for set 3. However higher prediction error of

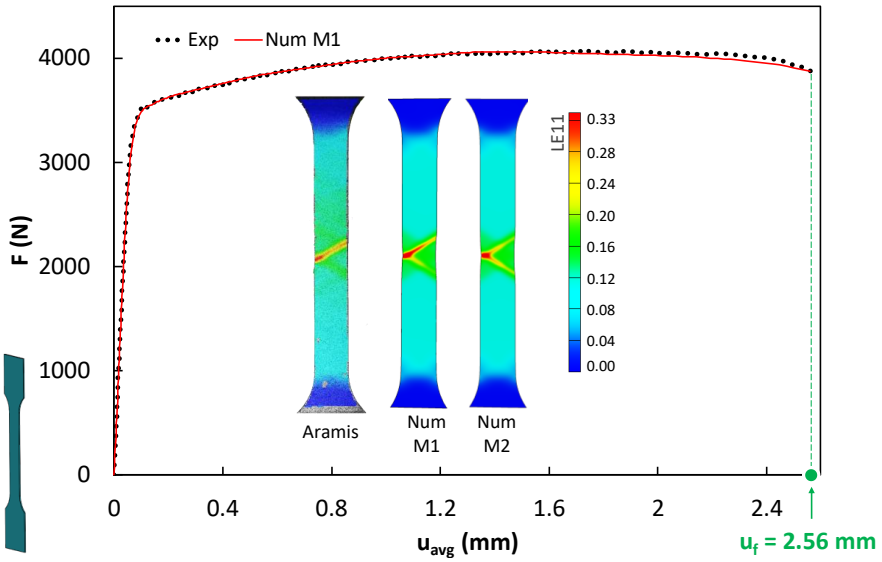

Figure 12: Comparison of the load-local displacement curves and the longitudinal logarithmic strain LE11 distributions on the specimen surface just before fracture for tensile specimen between numerical and experimental results.

about 7.23 % is found for model M2. This indicates again that model M1 is more suited than model M2 for the calibration of ductile fracture criterion which further validates the obtained results.

4. Conclusion

In this study, the hybrid experimental-numerical approach is used to calibrate Lou's fracture criterion for AA6061-T6 aluminum alloy. Special emphasis is put on the influence of boundary conditions on the accuracy prediction of this approach. To this end, numerical simulations are carried out with and without considering some experimental aspects like misalignment of specimen. The comparison between models and experiments shows that the

model constrained by experimental boundary conditions describes more precisely the deformation processes of the fracture tests. Moreover, it is found that experimental boundary conditions have a significant effect on the fracture strain and minor influence on the stress states (i.e stress triaxiality and Lode parameter). In addition, the effect of the calibration test is investigated. It is found that all sets of fracture tests leads to highly accurate results with model correctly constrained. The obtained results are verified using tensile test performed until fracture which confirms that model correctly constrained is more suited for calibration of ductile fracture criterion.

Acknowledgements

The authors acknowledge the Région Bretagne financial support with the SAD18037 program.

References

[1] M. Cockroft, D. Latham, Ductility and workability of metals, Journal of the Institute of Metals 96 (1968) 33–39.

[2] S. I. Oh, C. C. Chen, S. Kobayashi, Ductile fracture in axisymmetric extrusion and drawing—part 2: Workability in extrusion and drawing, Journal of Engineering for Industry 101 (1) (1979) 36–44. doi:10.1115/1.3439471.

[3] S. Clift, P. Hartley, C. Sturgess, G. Rowe, Fracture prediction in plastic deformation processes, International Journal of Mechanical Sciences 32 (1) (1990) 1–17. doi:10.1016/0020-7403(90)90148-c.

[4] P. Brozzo, B. Deluca, R. Rendina, A new method for the prediction of formability limits in metal sheets, in: Proc. 7th Biennial Conf. IDDRG, 1972.

[5] J. Rice, D. Tracey, On the ductile enlargement of voids in triaxial stress fields, Journal of the Mechanics and Physics of Solids 17 (3) (1969) 201–217. doi:10.1016/0022-5096(69)90033-7.

[6] M. Oyane, Criteria of ductile fracture strain, Bulletin of JSME 15 (90) (1972) 1507–1513. doi:10.1299/jsme1958.15.1507.

[7] M. Ayada, T. Higashino, K. Mori, Central bursting in extrusion of inhomogeneous materials, Advanced Technology of Plasticity 1 (1987) 553–558.

[8] Y. Ko, J. Lee, H. Huh, H. Kim, S. Park, Prediction of fracture in hub-hole expanding process using a new ductile fracture criterion, Journal of Materials Processing Technology 187-188 (2007) 358–362. doi:10.1016/j.jmatprotec.2006.11.071.

[9] A. Mishra, S. Thuillier, Investigation of the rupture in tension and bending of DP980 steel sheet, International Journal of Mechanical Sciences 84 (2014) 171–181. doi:10.1016/j.ijmecsci.2014.04.023.

[10] K. B. Othmen, N. Haddar, A. Jegat, P.-Y. Manach, K. Elleuch, Ductile fracture of AISI 304l stainless steel sheet in stretching, International Journal of Mechanical Sciences 172 (2020) 105404. doi:10.1016/j.ijmecsci.2019.105404.

[11] Y. Bao, T. Wierzbicki, A comparative study on various ductile crack formation criteria, Journal of Engineering Materials and Technology 126 (3) (2004) 314–324. doi:10.1115/1.1755244.

[12] I. Barsoum, J. Faleskog, Rupture mechanisms in combined tension and shear—experiments, International Journal of Solids and Structures 44 (6) (2007) 1768–1786. doi:10.1016/j.ijsolstr.2006.09.031.

[13] T. Wierzbicki, Y. Bao, Y.-W. Lee, Y. Bai, Calibration and evaluation of seven fracture models, International Journal of Mechanical Sciences 47 (4-5) (2005) 719–743. doi:10.1016/j.ijmecsci.2005.03.003.

[14] X. Gao, J. Kim, Modeling of ductile fracture: Significance of void coalescence, International Journal of Solids and Structures 43 (20) (2006) 6277–6293. doi:10.1016/j.ijsolstr.2005.08.008.

[15] Y. Bai, T. Wierzbicki, A new model of metal plasticity and fracture with pressure and Lode dependence, International Journal of Plasticity 24 (6) (2008) 1071–1096. doi:10.1016/j.ijplas.2007.09.004.

[16] Y. Bai, T. Wierzbicki, Application of extended Mohr-Coulomb criterion to ductile fracture, International Journal of Fracture 161 (1) (2010) 1–20. doi:10.1007/s10704-009-9422-8.

[17] D. Mohr, S. J. Marcadet, Micromechanically-motivated phenomenological Hosford–Coulomb model for predicting ductile fracture initiation at low stress triaxialities, International Journal of Solids and Structures 67-68 (2015) 40–55. doi:10.1016/j.ijsolstr.2015.02.024.

[18] Y. Lou, H. Huh, S. Lim, K. Pack, New ductile fracture criterion for prediction of fracture forming limit diagrams of sheet metals, International Journal of Solids and Structures 49 (25) (2012) 3605–3615. doi:10.1016/j.ijsolstr.2012.02.016.

[19] Y. Lou, H. Huh, Extension of a shear-controlled ductile fracture model considering the stress triaxiality and the Lode parameter, International Journal of Solids and Structures 50 (2) (2013) 447–455. doi:10.1016/j.ijsolstr.2012.10.007.

[20] Y. Lou, A new ductile fracture criterion for the formability prediction of steel sheets and its application to finite element analysis, Ph.D. thesis (08 2012).

[21] L. Mu, Y. Zang, Y. Wang, X. L. Li, P. M. A. Stemler, Phenomenological uncoupled ductile fracture model considering different void deformation modes for sheet metal forming, International Journal of Mechanical Sciences 141 (2018) 408–423. doi:10.1016/j.ijmecsci.2018.04.025.

[22] Y. Lou, H. Huh, Prediction of ductile fracture for advanced high strength steel with a new criterion: Experiments and simulation, Journal of Materials Processing Technology 213 (8) (2013) 1284–1302. doi:10.1016/j.jmatprotec.2013.03.001.

[23] A. D. Deole, M. R. Barnett, M. Weiss, The numerical prediction of ductile fracture of martensitic steel in roll forming, International Journal of Solids and Structures 144-145 (2018) 20–31. doi:10.1016/j.ijsolstr.2018.04.011.

[24] N. Habibi, A. Zarei-Hanzaki, H.-R. Abedi, An investigation into the fracture mechanisms of twinning-induced-plasticity steel sheets under various strain paths, Journal of Materials Processing Technology 224 (2015) 102–116. doi:10.1016/j.jmatprotec.2015.04.014.

[25] S. J. Zhang, Y. C. Lu, Z. H. Shen, C. Zhou, The effect of various notches on the prediction of the ductile fracture for SUS304 sheets, Key Engineering Materials 794 (2019) 36–41. doi:10.4028/www.scientific.net/kem.794.36.

[26] S. Baltic, J. Magnien, H.-P. Gänser, T. Antretter, R. Hammer, Coupled damage variable based on fracture locus: Modelling and calibration, International Journal of Plasticity 126 (2020) 102623. doi:10.1016/j.ijplas.2019.11.002.

[27] Y. Lou, L. Chen, T. Clausmeyer, A. E. Tekkaya, J. W. Yoon, Modeling of ductile fracture from shear to balanced biaxial tension for sheet metals, International Journal of Solids and Structures 112 (2017) 169–184. doi:10.1016/j.ijsolstr.2016.11.034.

[28] S. Zhang, Y. Lu, Z. Shen, C. Zhou, Y. Lou, Prediction of ductile fracture for Al6016-T4 with a ductile fracture criterion: Experiment and simulation, International Journal of Damage Mechanicsdoi:10.1177/1056789519865771.

[29] X. Zhuang, T. Wang, X. Zhu, Z. Zhao, Calibration and application of ductile fracture criterion under non-proportional loading condition,

Engineering Fracture Mechanics 165 (2016) 39–56. doi:10.1016/j.engfracmech.2016.08.021.

[30] Z. Yang, C. Zhao, G. Dong, Z. Chen, Y. Sun, X. Jia, Forming limit prediction of AA7075-T6 sheet based on ductile fracture criterion and the error analysis of parameters calibration, International Journal of Material Formingdoi:10.1007/s12289-019-01528-w.

[31] G. jiang DONG, Z. wei CHEN, Z. yun YANG, B. cheng FAN, Comparative study on forming limit prediction of AA7075-t6 sheet with M-K model and Lou-Huh criterion, Transactions of Nonferrous Metals Society of China 30 (6) (2020) 1463–1477. doi:10.1016/s1003-6326(20)65311-0.

[32] A. M. Beese, M. Luo, Y. Li, Y. Bai, T. Wierzbicki, Partially coupled anisotropic fracture model for aluminum sheets, Engineering Fracture Mechanics 77 (7) (2010) 1128–1152. doi:10.1016/j.engfracmech.2010.02.024.

[33] Y. Lou, J. W. Yoon, Alternative approach to model ductile fracture by incorporating anisotropic yield function, International Journal of Solids and Structures 164 (2019) 12–24. doi:10.1016/j.ijsolstr.2019.01.011.

[34] B. Tang, F. Wu, Q. Wang, J. Liu, N. Guo, H. Ge, Q. Wang, P. Liu, Damage prediction of hot stamped boron steel 22MnB5 with a microscopic motivated ductile fracture criterion: Experiment and simula-

tion, International Journal of Mechanical Sciences 169 (2020) 105302–. doi:10.1016/j.ijmecsci.2019.105302.

[35] G. Gruben, D. Morin, M. Langseth, O. Hopperstad, Strain localization and ductile fracture in advanced high-strength steel sheets, European Journal of Mechanics - A/Solids 61 (2017) 315–329. doi:10.1016/j.euromechsol.2016.09.014.

[36] GOM mbH , Aramis user manual software, 2007.

[37] J. Li, F. Li, Y. Cui, Effect of notch radius on anisotropic fracture response of AA6061-t6 under tension process, Theoretical and Applied Fracture Mechanics 103 (2019) 102276. doi:10.1016/j.tafmec.2019.102276.

[38] M. Dunand, D. Mohr, Hybrid experimental–numerical analysis of basic ductile fracture experiments for sheet metals, International Journal of Solids and Structures 47 (9) (2010) 1130–1143. doi:10.1016/j.ijsolstr.2009.12.011.

[39] Y. Lou, J. W. Yoon, H. Huh, Q. Chao, J.-H. Song, Correlation of the maximum shear stress with micro-mechanisms of ductile fracture for metals with high strength-to-weight ratio, International Journal of Mechanical Sciences 146-147 (2018) 583–601. doi:10.1016/j.ijmecsci.2018.03.025.

[40] A. Kacem, A. Krichen, P.-Y. Manach, S. Thuillier, J.-W. Yoon, Failure prediction in the hole-flanging process of aluminium alloys, Engineering

Fracture Mechanics 99 (2013) 251–265. doi:10.1016/j.engfracmech.2012.12.018.

[41] H. Talebi-Ghadikolaee, H. M. Naeini, M. J. Mirnia, M. A. Mirzai, H. Gorji, S. Alexandrov, Fracture analysis on U-bending of AA6061 aluminum alloy sheet using phenomenological ductile fracture criteria, Thin-Walled Structures 148 (2020) 106566. doi:10.1016/j.tws.2019.106566.

[42] V. Tarigopula, O. S. Hopperstad, M. Langseth, A. H. Clausen, F. Hild, O.-G. Lademo, M. Eriksson, A study of large plastic deformations in dual phase steel using digital image correlation and FE analysis, Experimental Mechanics 48 (2) (2007) 181–196. doi:10.1007/s11340-007-9066-4.

[43] H. Quach, J.-J. Kim, D.-T. Nguyen, Y.-S. Kim, Uncoupled ductile fracture criterion considering secondary void band behaviors for failure prediction in sheet metal forming, International Journal of Mechanical Sciences 169 (2020) 105297. doi:10.1016/j.ijmecsci.2019.105297.

[44] D. Mohr, S. Henn, Calibration of stress-triaxiality dependent crack formation criteria: A new hybrid experimental–numerical method, Experimental Mechanics 47 (6) (2007) 805–820. doi:10.1007/s11340-007-9039-7.

[45] Y. Bai, X. Teng, T. Wierzbicki, On the application of stress triaxiality formula for plane strain fracture testing, Journal of Engineering Materials and Technology 131 (2). doi:10.1115/1.3078390.

[46] X. Gao, T. Zhang, M. Hayden, C. Roe, Effects of the stress state on plasticity and ductile failure of an aluminum 5083 alloy, International Journal of Plasticity 25 (12) (2009) 2366–2382. doi:10.1016/j.ijplas.2009.03.006.

[47] L.-Y. Qian, G. Fang, P. Zeng, Q. Wang, Experimental and numerical investigations into the ductile fracture during the forming of flat-rolled 5083-O aluminum alloy sheet, Journal of Materials Processing Technology 220 (2015) 264–275. doi:10.1016/j.jmatprotec.2015.01.031.